

Spincopter Wing Design and Flight Control

Matko Orsag · Josip Cestic · Tomislav Haus ·
Stjepan Bogdan

Received: 30 June 2012 / Accepted: 12 July 2012 / Published online: 12 August 2012
© Springer Science+Business Media B.V. 2012

Abstract This paper presents dynamical properties of an unmanned aerial vehicle (UAV), called spincopter. The vehicle structure is based on two wings that are forced in rotation (spinning) by propulsion system formed of two propellers. Based on devised dynamical model, that reveals inherent stability of the vehicle, composition of control algorithms for vertical and horizontal movement is proposed. Due to the specific configuration of the propulsion system, movement in horizontal direction is produced by pulsations in rotational speed of propulsion motors. An analysis of influence that such a configuration has on the vehicle dynamics is given. Finally, design recommendations for rotational wings are elaborated, based on extensive simulations of spincopter by using X-Plane® software package.

Keywords UAV · Rotorcraft · Control · Aerodynamics

1 Introduction

Rapid development of actuators on μm level (MEMS and Piezo technology) provided background for design of very small bioinspired unmanned aerial vehicles (UAVs) [1, 2]. Miniaturization of UAVs went from micro design to pico design stage [3]. This new tendency requires a shift in UAV concept philosophy. Rotorcraft and fixed wing propulsion systems, used in classical approach, are replaced by flapped [4] and spinning wings [5, 6], thus making UAV designs even more alike to living organisms [7]. Although broad research of flight phenomena encountered in nature date in the late 70's [8] and early 80's [9, 10], powerful computational tools, on the software and hardware level, just recently provided deep insight into physics of movable wings [11–13] and low Reynolds number flow regime. This, detailed, analysis sheds new light on efficiency of the two prevailing concepts (i.e. rotary and flapping designs [14]), which is of the outmost importance due to the limited energy resource carried by an UAV. Furthermore, as energy efficiency is closely related to the wing shape, obtained results are used not only as proofs of new concepts, but also as blueprints for design of novel wing profiles and shapes.

M. Orsag (✉) · J. Cestic · T. Haus · S. Bogdan
Laboratory for Robotics and Intelligent Control
Systems, Faculty of Electrical Engineering and
Computing, University of Zagreb,
Unska 3, 10000 Zagreb, Croatia
e-mail: matko.orsag@fer.hr

J. Cestic
e-mail: josip.cestic@fer.hr

T. Haus
e-mail: tomislav.haus@fer.hr

S. Bogdan
e-mail: stjepan.bogdan@fer.hr

As debate regarding efficiency of two concepts continues, research community began investigation on control techniques that should allow controllability of newly designed UAV. The most explored UAV model, based on rotary wing, is the one that furnishes a wing mimicking a maple seed, so called Samara concept [15, 16]. Based on a single rotating wing with only two actuators, this UAV, although inherently stable, is under-actuated, nonlinear and has coupled variables, which makes it a challenging object from the control point of view. Although manual control of such a UAV, due to its inherent stability, is not demanding as manual control of helicopters and quadrotors, implementation of autonomous flight is rather difficult since all feedback signals are acquired from sensors that are located in the vehicle's rotating coordinate system.

A work presented in this paper is continuation of research described in [17]. The paper is structured in the following way. In Section 2, a mathematical model of the vehicle is described. Instead of using one wing, spincopter concept is based on two rotating wings. The benefit of such a concept is twofold: firstly, two wings produce more lift (thorough analysis of influence that wing shape has on the lift is given in Section 4), and secondly the stability of the vehicle is further enhanced (some experiments with UAVs based on one rotating wing demonstrate degradation of the stability at low rotational speeds). Two actuators, placed symmetrically with respect to the center of gravity of the vehicle, are used to generate thrust which spins the wings that in effect produce lift. As it is demonstrated in Section 3, difference in thrust, produced by pulsations in rotational speeds of propulsion motors, is used to control the vehicle velocity in the horizontal plane. Concluding remarks and directions for future work are given in the last section of the paper.

2 Mathematical Model of Flight Dynamics

A spincopter, depicted in Fig. 1, is a flying vehicle comprised of two wings, a fuselage and two propulsors. The fuselage contains an energy source and the required electronics. The propulsors, driven by dc motors, are positioned on the

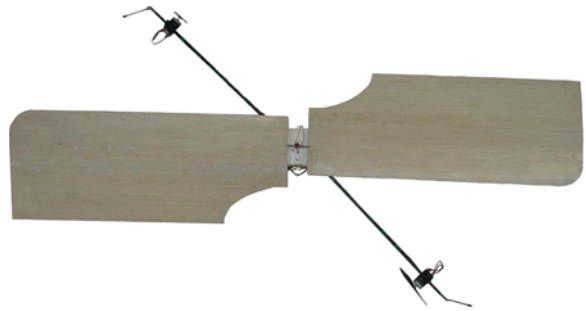


Fig. 1 A spincopter

opposite sides of the fuselage, equally distanced from the machine's rotation axis and attached to a tiny tube. Construction symmetry ensures that flyer's rotation axis passes through its COG. Each propulsor, composed of two blades, produces thrust that causes torque, which in turn spins the vehicle.

While spinning, the wings produce lift, thus causing vertical movement of the flyer [17] (Fig. 2). The theory and experimental research of aerodynamics are focused on balancing the lift/drag ratio (L/D ratio), which is an efficiency factor for aircraft design (wing and airfoil designs are elaborated in Section 4).

Mathematical model, presented herein, represents the first approximation of the flyer's physics, including a few essential aerodynamic influences.

2.1 Vertical Movement

The basic differential equation describing the relation between a rotational propulsor speed and dc motor voltage is given as

$$T_{\omega p} \frac{d\omega_p}{dt} + \omega_p = k_{\omega p} \cdot U_{dc} \quad (1)$$

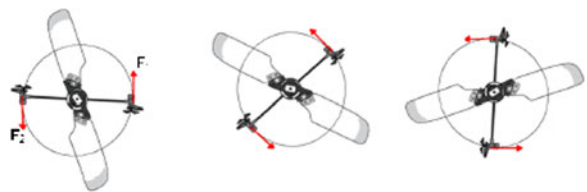


Fig. 2 Spinning caused by the propulsors' thrust [17]

where ω_p is the rotational propulsor speed, $T_{\omega p}$ is the dc motor time constant, $k_{\omega p}$ is the dc motor gain and U_{dc} is the dc motor voltage [18].

The two propulsors generate torque in addition to the thrust F , which can be calculated using:

$$F = k_f \cdot \omega_p^2 \quad (2)$$

where k_f represents the thrust coefficient [18].

Rotational speed of the flyer, ω_z , is determined from

$$I_z \frac{d\omega_z}{dt} = (F_1 + F_2) \cdot R_p - k_{d\omega} \cdot \omega_z^2 \quad (3)$$

where F_1 and F_2 are the thrusts caused by motor 1 and motor 2, I_z is the rotational moment of inertia of the flyer, R_p is the distance between the propulsor and the spirocopter's COG and $k_{d\omega}$ is the drag coefficient.

Finally, the shift in z direction is calculated as

$$m \frac{d^2 z}{dt^2} = k_{l\omega} \cdot \omega_z^2 - m \cdot g - k_z \frac{dz}{dt} \quad (4)$$

where m is the mass of the spirocopter, g is the gravitational constant, k_z is the friction coefficient in z direction and $k_{l\omega}$ is the lift coefficient.

In Eqs. 3 and 4, the connection between the overall thrust ($F_1 + F_2$) and vertical velocity is defined. Their responses, for $T_{\omega p} = 0[s]$, are shown in Fig. 3.

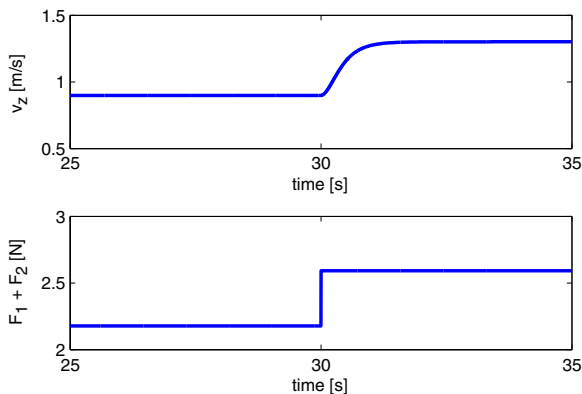


Fig. 3 The vertical movement

2.2 Horizontal Movement

System dynamics in an x-y plane are described by second order differential equations:

$$\begin{aligned} m \frac{d^2 x}{dt^2} &= F_x(t) - k_x \frac{dx}{dt} \\ m \frac{d^2 y}{dt^2} &= F_y(t) - k_y \frac{dy}{dt} \end{aligned} \quad (5)$$

where F_x and F_y represent the current forces in positive x and y directions, k_x and k_y are the friction coefficients in x and y directions.

Figure 4 depicts force vectors in a ground frame of reference, produced by each propulsor, at a particular moment t, where φ is the angle between x-axis and 1st propulsor. Therefore, the angle between the position of the 1st propulsor and the force produced by the same motor is 90° , while the angular position is measured as the position of motor 1.

Deriving from Fig. 4, current forces in x and y directions produced by thrusts of each propulsor (F_1 and F_2) are

$$F_x(t) = [-F_1(t) + F_2(t)] \cdot \sin(\omega_z t)$$

$$F_y(t) = [F_1(t) - F_2(t)] \cdot \cos(\omega_z t) \quad (6)$$

After taking off, the spirocopter keeps its horizontal position as long as the difference between F_1 and F_2 is zero. If we assume that $F_1 = F_2$ and $\omega_z = \text{const.}$, the average force generated in the

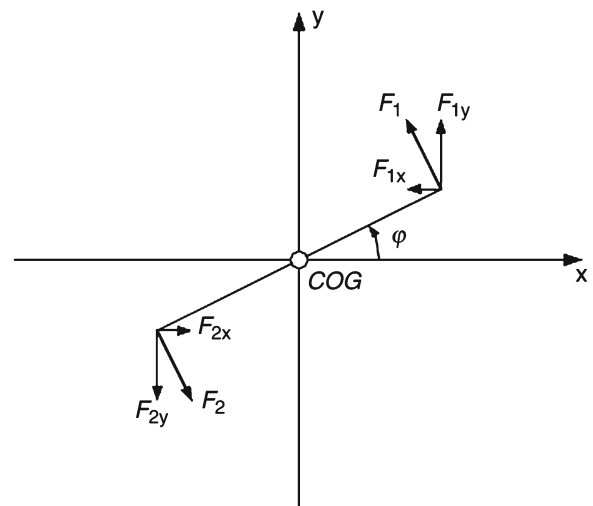
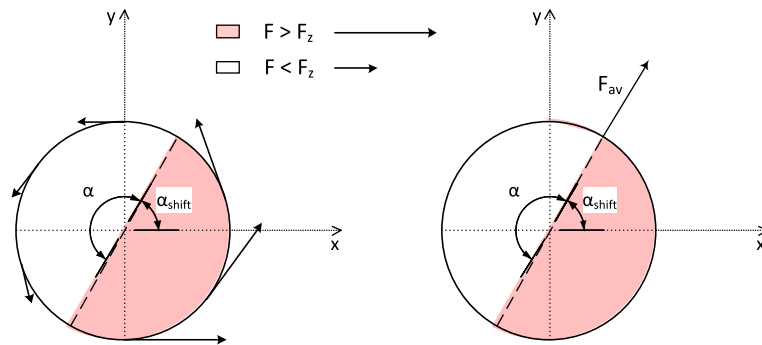


Fig. 4 Forces that cause a horizontal movement [17]

Fig. 5 Horizontal force produced by the disbalance of the thrust forces F of each propulsor



positive direction of the x-axis for one full rotation of the flyer is given with

$$F_{x,av} = \frac{1}{T} \int_{t_0}^{t_0+T} F_x(t) dt = \frac{1}{2\pi} \int_{\alpha_0}^{\alpha_0+2\pi} F_x(\varphi) d\varphi = 0 \quad (7)$$

where T represents the period of rotation. The same holds for the force in the positive direction of the y-axis:

$$F_{y,av} = \frac{1}{T} \int_{t_0}^{t_0+T} F_y(t) dt = \frac{1}{2\pi} \int_{\alpha_0}^{\alpha_0+2\pi} F_y(\varphi) d\varphi = 0 \quad (8)$$

In order to achieve horizontal movement, the difference between F_1 and F_2 must be a non-zero value. For $T_{\omega p} = 0[s]$, the speed of the propulsors can be immediately changed for a particular time period $[t_1, t_2]$ such that $t_1 \leq t_2 \leq t_1 + T$. Written with respect to the angles $[\alpha = \varphi(t_1), \beta = \varphi(t_2)]$ such that $0 < \alpha \leq \beta \leq \alpha + 360^\circ$, the average values of F_x and F_y become

$$\begin{aligned} F_{x,av} &= \frac{-F_1 + F_2}{2\pi} \int_{\alpha}^{\beta} \sin(\varphi) d\varphi \\ &= \frac{F_1 - F_2}{2\pi} [\cos(\beta) - \cos(\alpha)] \\ F_{y,av} &= \frac{F_1 - F_2}{2\pi} \int_{\alpha}^{\beta} \cos(\varphi) d\varphi \\ &= \frac{F_1 - F_2}{2\pi} [\sin(\beta) - \sin(\alpha)] \end{aligned} \quad (9)$$

From Eq. 9, the interval $[\alpha, \beta]$ with duration of 180° ensures the largest effect on the resultant force, which produces horizontal movement. The resultant force is

$$\mathbf{F}_{av} = \sqrt{F_{x,av}^2 + F_{y,av}^2} \cdot e^{i\alpha_{shift}} \quad (10)$$

where α_{shift} is the angle of movement in x-y plane. As depicted in Fig. 5, to achieve the movement in the α_{shift} direction, it is necessary to decrease the thrust beneath the value of F_z within the interval $[0, 180^\circ]$, and increase it over F_z in the interval $[180^\circ, 360^\circ]$, with respect to α_{shift} . F_z stands for an average value of thrust, produced by the propulsors in order to achieve the desired vertical movement.

In order to decrease the load on dc motors, the added thrusts which produce the shift in the x-y plane are always positive for motor 1 and negative for motor 2. Hence, the simple responses of the thrusts and angular position, as well as the horizontal velocities are depicted in Figs. 6 and 7, respectively.

It is evident from Fig. 6 that the voltage response has two states. Figure 5 shows that the shift direction of α_{shift} fits the angle of the disbalanced area's end.

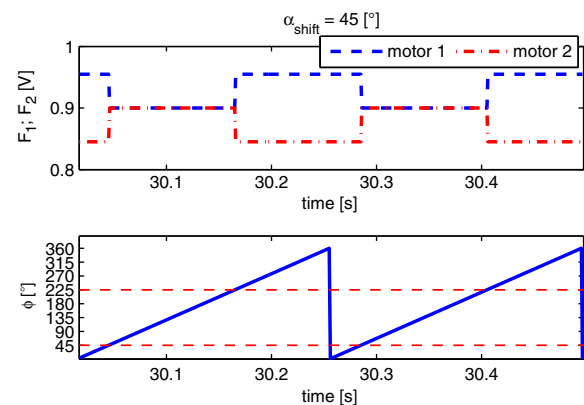


Fig. 6 The thrusts of each propulsor and current position of motor 1; for $\alpha_{shift} = 45^\circ$

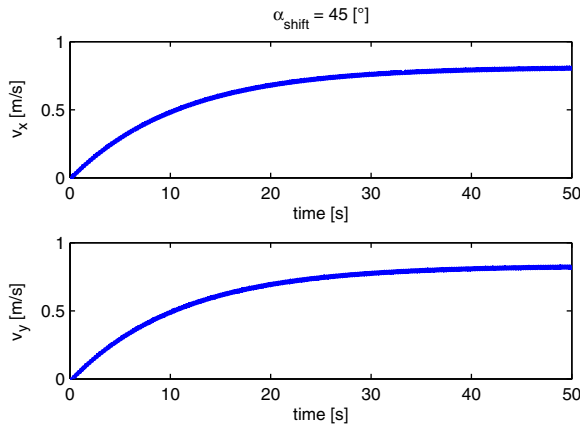


Fig. 7 The velocity components v_x and v_y ; for $\alpha_{\text{shift}} = 45^\circ$

A more complex model that includes the influence of $T_{op} \neq 0[s]$, is elaborated in Section 3.

2.3 Gyroscopic Stability

The key aspect of gyroscopic stability in the spincopter aircraft is the law of conservation of angular momentum. The law of conservation of angular momentum states that the angular momentum of an object remains constant as long as no external torques, or moments, act on it. The derivations presented herein resembles the similar effect observed in a frisbee [19]. We consider spincopter hovering with a constant angular velocity $\omega_z = \Omega_z$, and therefore a constant angular momentum L_z . Furthermore, we consider spincopter to be symmetrical and define principal axis x , y and z , with respective moments of inertia I_{xx} , I_{yy} and I_{zz} . Keeping in mind that the yaw rotation speed ω_z is constant, a simplified set of Euler Rigid body motion equations can be written:

$$I_{xx}\dot{\omega}_x + K_{dx}\omega_x = M_x - (I_{zz} - I_{yy})\omega_y\omega_z \quad (11a)$$

$$I_{yy}\dot{\omega}_y + K_{dy}\omega_y = M_y - (I_{xx} - I_{zz})\omega_x\omega_z \quad (11b)$$

$$\omega_z = \Omega_z \quad (11c)$$

where K_{dx} and K_{dy} represent a simplified, linearized drag coefficients (i.e. $F_D = k_\delta \omega^2 \mapsto K_D \Delta\omega|_{\omega_0}$). Considering a wind gust as a torque impulse acting only on roll axis M_x , we can solve the above equations for rotation speeds ω_x and ω_y . The same analysis can be applied to pitch angle dynamics. Under the assumption of small

drag coefficients (i.e. $K_{dx}K_{dy} \ll$), the following transfer functions can be derived:

$$\omega_x(s) = \frac{M_x(s)}{I_{xx}} \frac{s + \frac{K_{dy}}{I_{yy}}}{s^2 + K_1s + K_2\Omega_z^2} \quad (12a)$$

$$\omega_y(s) = \frac{M_x(s)}{I_{xx}I_{yy}} \frac{(I_{zz} - I_{xx})\Omega_z}{s^2 + K_1s + K_2\Omega_z^2} \quad (12b)$$

where coefficients K_1 and K_2 are:

$$K_1 = \frac{K_{dy}}{I_{yy}} + \frac{K_{dx}}{I_{xx}} \quad (13a)$$

$$K_2 = \frac{(I_{zz} - I_{xx})(I_{zz} - I_{yy})}{I_{xx}I_{yy}} \quad (13b)$$

Three main conclusions can be derived from previous transfer function: stability, steady state and oscillatory behavior. Poles of the characteristic polynomial of the system are:

$$-\frac{K_1}{2} \pm \sqrt{\frac{K_1^2}{4} - K_2\Omega_z^2} \quad (14)$$

Under the assumption of small drag coefficients $K_1^2, K_1 \ll 4K_2\Omega_z^2$, the necessary stability criteria dictates that the principal moments of inertia satisfy one of the two following conditions: $I_{zz} > I_{xx} \wedge I_{zz} > I_{yy}$ or $I_{zz} < I_{xx} \wedge I_{zz} < I_{yy}$. That way, $K_1 > 0$ and the system behaves as a filter for wind gust torques. Due to the construction characteristics of the spincopter I_{zz} is the largest principal moment of inertia, so that the first condition is met. For a steady state conditions (i.e. $\lim_{s \rightarrow 0}$) rotation speed transfer functions take the following form:

$$\omega_x \sim \frac{K_{dy}}{I_{xx}I_{yy}K_2\Omega_z^2} \quad (15a)$$

$$\omega_y \sim \frac{(I_{zz} - I_{xx})}{I_{xx}I_{yy}K_2\Omega_z^2} \quad (15b)$$

This implies that as the rotation speed Ω_z increases, so does the attenuation of applied wind gust disturbances. Consequently, this shows that the vehicle becomes more stable as the rotation speed increases. Equation 14 also shows that the increase of rotation speed Ω_z increases the frequency of oscillations by increasing the imaginary part of the two characteristic poles.

As the consequence of oscillations caused by wind gusts the vehicle will start to ‘wobble’, i.e.

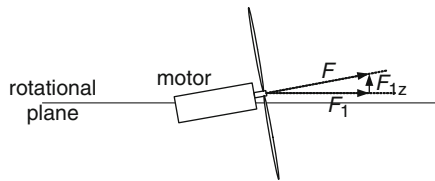


Fig. 8 Roll angle control: motor axle closes a 5° with the rotation plane

gyroscopic precession will take effect. The same phenomenon could be caused by slight imperfections in wings' design. Any deficiency will induce different lift forces on right and left wing. In turn, torque produced by such a difference in lift forces will increase/decrease roll angle of the vehicle and spin axis will start to change its orientation, in effect describing a cone shape trajectory. Clearly, such behavior of the vehicle is detrimental.

However, a slight modification to the spirocopter construction, shown in Fig. 8 can stabilize the precession of the vehicle. As the lift force of the wing depends on the angle of attack, which corresponds with the pitch angle of the vehicle, a slight change of pitch angle will change the angle of attack. By varying the angle of attack of the wings, we can consequently cancel out the aerodynamic difference between the wings and in turn trim the precession down. In order to control the roll, the angle of motors' axle with respect to the rotational plane (Fig. 8) is slightly increased (in our case for 5°). This modification introduces new force in direction of z axis. New force generates torque acting on vehicle's pitch, thus directly changing the angle of attack of the wings.

2.4 Controller Structure

Previously mentioned modification to the spirocopter construction, allows us to control spirocopter speed in a 3D space, as well as the roll angle of the aircraft. Controller structure is shown in Fig. 9, with separate loops for horizontal speed, vertical speed and roll angle.

For the purpose of manipulating spirocopter's vertical speed a PI-type controller, which calculates the voltage level U_z , was chosen. Comparing Eqs. 3 and 9, it is obvious that the control loops for the vertical and horizontal movements are coupled [17].

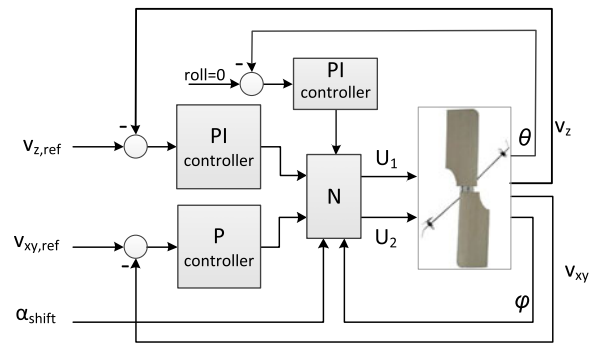


Fig. 9 Controller structure

From Eq. 9 it follows that the average value of the horizontal forces can be affected by any of the following variables; F_1 , F_2 , α or β . In order to keep the controller simple, the method proposed herein achieves the required horizontal force by altering the disbalance between F_1 and F_2 , while keeping the difference $\beta - \alpha = 180^\circ$ constant, as depicted earlier. More complex control algorithms are considered in Section 3.

In order to manipulate spirocopter's horizontal speed a simple P-type controller was used. While determining the voltage contributions for the x-y plane control, it is important that the value of $F_1 + F_2$ remains unchanged (with respect to $F \propto U^2$). Therefore, the P-type controller determines the voltage contribution for motor 1 which increases its voltage whenever the control error is a non-zero value.

$$\Delta U_{1,xy} = K_{c,xy} \cdot |v_{xy,r} - v_{xy}| \quad (16)$$

where $K_{c,xy}$ is the P-type regulator gain, $v_{xy,r}$ is the reference speed in an x-y plane, v_{xy} is the current speed in an x-y plane and $\Delta U_{1,xy}$ is the voltage contribution for motor 1.

Afterwards, the voltage contribution for motor 2 has a nonlinear functional dependence. Finally, the voltage levels for motor 1 and motor 2, U_1 and U_2 , are calculated in the nonlinear element N as

$$U_1 = \begin{cases} U_z & ; \phi \notin [\alpha, \beta] \\ U_z + \Delta U_{1,xy} & ; \phi \in [\alpha, \beta] \end{cases}$$

$$U_2 = \begin{cases} U_z & ; \psi \notin [\alpha + 180^\circ, \beta + 180^\circ] \\ U_z + f(\Delta U_{1,xy}) & ; \psi \in [\alpha + 180^\circ, \beta + 180^\circ] \end{cases} \quad (17)$$

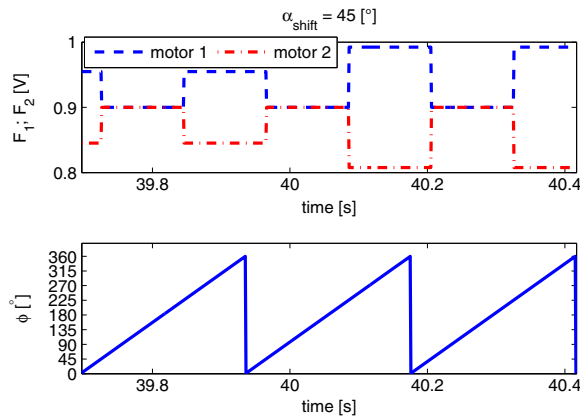


Fig. 10 The thrusts of each propulsor and current position of motor 1; for $\alpha_{shift} = 45^\circ$

where α depicts the beginning of pulsation of motor 1, β depicts the ending of pulsation of motor 1, ψ is the angular position of motor 2 and $f(\Delta U_{1,xy})$ represents the nonlinear voltage contribution for motor 2. In order to keep the sum $F_1 + F_2$ unchanged, with respect to nonlinear characteristic $F \propto U^2$, $f(\Delta U_{1,xy})$ is negative. The angle of 180° , added to motor 2, fits its position with respect to motor 1.

With tilted motor axes it is possible to apply torque to correct the roll angle of the vehicle. A simple PI controller, shown in Fig. 9 varies the speed of motors. This in turn adjusts the wing's angle of attack which finally corrects the orientation of the aircraft.

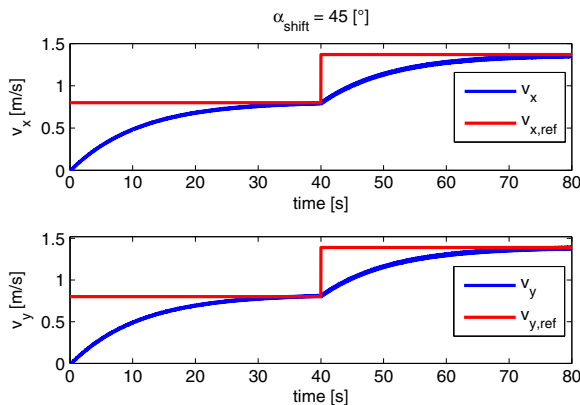


Fig. 11 The velocity components v_x and v_y ; for $\alpha_{shift} = 45^\circ$

In Figs. 10 and 11, the responses of the motors' thrusts and current angular position, as well as the horizontal velocities are shown.

3 Flight Control Algorithm

To ensure satisfactory mobility of the spirocopter, it's necessary to determine the most efficient control algorithm. While the vertical movement requires the change in average motor thrusts, the horizontal movement, as depicted earlier, requires more complex control algorithms including motor pulsations. Therefore, the motor dynamics has a vital influence on flyer's dynamic behaviour. In this paper, several approaches were considered.

3.1 The Pulsation Period

The basic idea of the experiments was to examine a pulsation through multiple turns, given varying dc motor time constants. The average values of the forces in x and y directions are

$$F_{x,av} = \frac{1}{kT} \int_{t_0}^{t_0+kT} F_x(t) dt = \frac{1}{k \cdot 2\pi} \int_{\alpha_0}^{\alpha_0+k \cdot 2\pi} F_x(\varphi) d\varphi$$

$$F_{y,av} = \frac{1}{kT} \int_{t_0}^{t_0+kT} F_y(t) dt = \frac{1}{k \cdot 2\pi} \int_{\alpha_0}^{\alpha_0+k \cdot 2\pi} F_y(\varphi) d\varphi$$
(18)

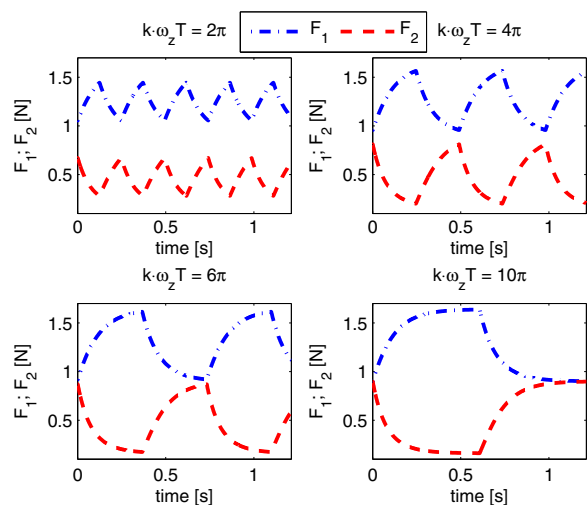


Fig. 12 Thrust responses for different pulsation periods; with $T_{op} = 0.105[s]$

where k represents the number of vehicle turns during one pulsation period. The final purpose of the research is to maximize the average force that affects the flyer's horizontal movement.

$$|\mathbf{F}_{av}| = \sqrt{F_{x,av}^2 + F_{y,av}^2} \quad (19)$$

Since the analytical solution of Eq. 18 is a composite multivariate function, it is more practical to use a simulation package, such as Simulink®. In the simulations the behaviour of the flyer was tested using three different dc motor time constants, the one that belongs to the real drives of the spincopter, $T_{op} = 0.105[s]$, and two other; $3 \cdot T_{op} = 0.315[s]$ and $1/3 \cdot T_{op} = 0.035[s]$.

The average force (Eq. 19) has a direct impact on the horizontal speed. Because of this, the max-

Table 1 The maximum speed in x-y plane

	$k \cdot \omega_z T$	2π	$3 \cdot 2\pi$	$5 \cdot 2\pi$
T_{op}	$= 0.105[s]$	5[m/s]	1.8	1.1
$3T_{op}$	$= 0.315[s]$	1.9	0.65	0.4
$1/3T_{op}$	$= 0.035[s]$	11.2	4	2.5

imum speed reached in x-y plane, using the same controller output, was used as the quality criteria for different approaches in the horizontal control. During the simulations, the open loop control of the vertical movement was sufficient and the vertical component of the voltage was chosen as $U_z = U_{z,hov}$, where $U_{z,hov}$ is the voltage required for hovering.

Independent from the pulsation period, the simulation results were obtained using a maximum

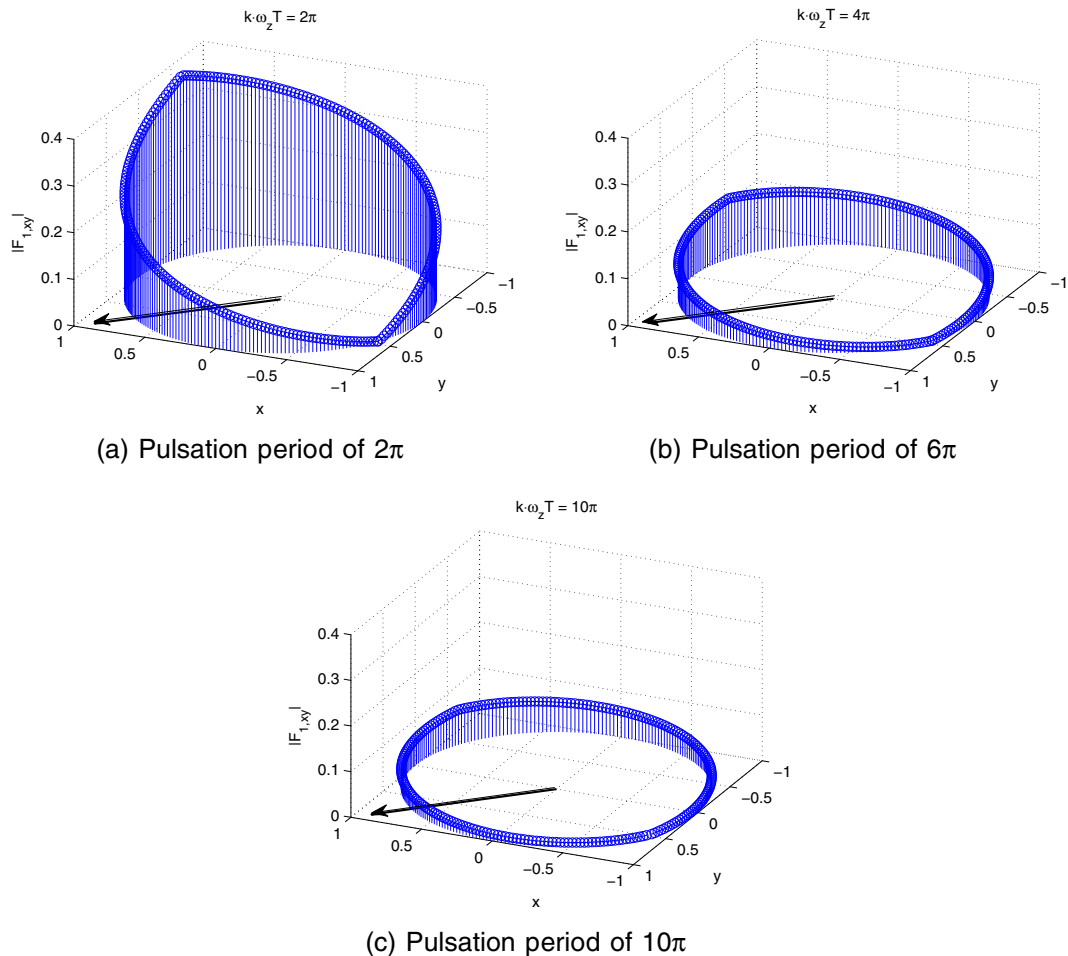


Fig. 13 The volatile component of the force produced by motor 1

allowed control signal (i.e. voltage difference). Thrust responses for pulsation periods of $\omega_z T = 2\pi$, $2 \cdot \omega_z T = 4\pi$, $3 \cdot \omega_z T = 6\pi$ and $5 \cdot \omega_z T = 10\pi$ (1, 2, 3 and 5 turns, respectively), using $T_{op} = 0.105[s]$, are shown in Fig. 12.

To achieve a significant movement in x-y plane, U_{xy} voltage has to be applied for an odd multiple of 180° . Otherwise, the average force is close to zero. Thus, the maximum speeds for the pulsation periods of $k \cdot \omega_z T = 2n \cdot 2\pi$; $n \in N$ are not used. The maximum velocities, according to different motor time constants and pulsation periods are given in Table 1.

In Table 1 it can be seen that the most efficient pulsation period is 360° and it is independent of the motor's time constant. The average contribution in the force, for different pulsation periods, that causes horizontal movement, produced by motor 1 is depicted in Fig. 13. The direction of the resultant force is marked with a black arrow ($\alpha_{\text{shift}} = 45^\circ$).

According to the obtained results, the pulsation period of 360° is chosen for the implementation on the spirocopter. Using the multiple turn pulsation approach, the varying component of the thrusts which causes horizontal movement was not large enough to compensate for the duration of the period.

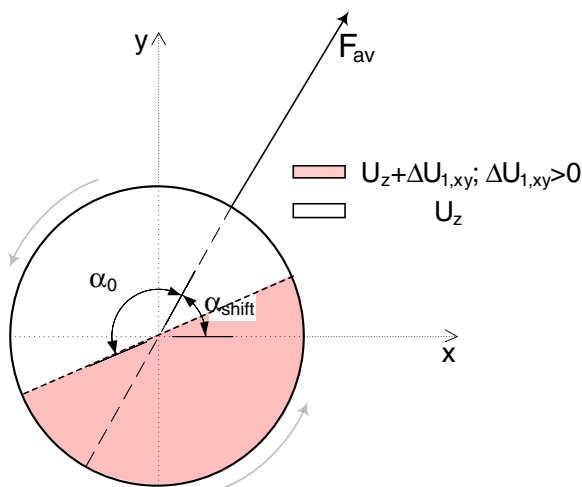


Fig. 14 The intervals of disbalanced voltages for motor 1; for pulsation period of 360°

Table 2 The beginning angle of pulsation

$n_z[rpm]$	170	200	230	250	260	275	296	330
$\alpha_0[^\circ]$	116	113	111	109	108	107	106	105

Bold entries mark the hovering speed.

3.2 The Interval of Disbalanced Voltages

For the chosen control approach with a pulsation period of 360° within the disbalanced voltages of each dc motor for half of the period, it is necessary to determine the angle of the start of pulsation. Due to the non-zero motor time constant, the interval of disbalanced voltages is different from the one depicted in Section 2.2. The voltage areas are shown in Fig. 14. In order to obtain an accurate behaviour depending on the angular velocity of the spirocopter, the angle α_0 (Fig. 14) is determined through simulations. The results for $T_{op} = 0.105[s]$, are given in Table 2.

To make it more suitable for implementation on a microcontroller or a simulator, the $n_z - \alpha_0$ relation is interpolated with a quadratic function, which accurately fits the measured points (depicted in Fig. 15):

$$\alpha_0 = 2.427 \cdot 10^{-4} \cdot n_z^2 - 0.1922 \cdot n_z + 141.7796 \quad (20)$$

The beginning of the pulsation interval affects the precision of movement in the x-y plane, while the pulsation period affects the flyer's mobility

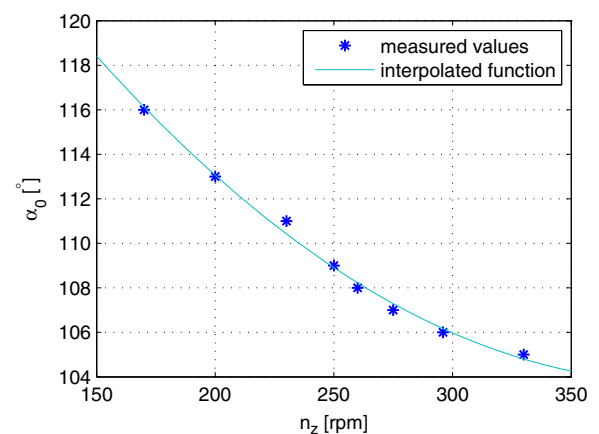


Fig. 15 The graphical representation of $n_z - \alpha_0$ relation and its interpolation

and its general behaviour. Due to the large dc motor time constant, it is necessary to investigate some other influences that affect the flyer's behaviour, such as wing design.

4 Wing Design

In order to achieve as good flight characteristics as possible, it is necessary to determine the optimal aerodynamic wing parameters. The mass and the moment of inertia also contribute to the overall characteristics of the spincopter. Thus, by using an appropriate model and a systematic approach to testing, it is possible to achieve the desired results. Testing was based on the basic laws of aerodynamics (i.e. proportional characteristics of lift with respect to squared velocity— $L \propto v^2$, and angle of attack— $L \propto \alpha_{AoA}$) [20]. In general, the designing process requires a construction of an airfoil and an estimation of the wing dimensions. Due to the enormous complexity of airfoil theory, airfoil parameters are usually determined experimentally and go beyond the scope of this paper. The airfoil chosen for the aircraft is optimized for low speed aircraft. Herein presented simulations were oriented towards finding the optimal wing shape and size, and investigating the influence these parameters have on the lift, drag, mass and moment of inertia.

4.1 X-Plane model of Spincopter

Although the X-Plane was originally designed as a flight simulator game, during time it became a comprehensive and powerful engineering tool

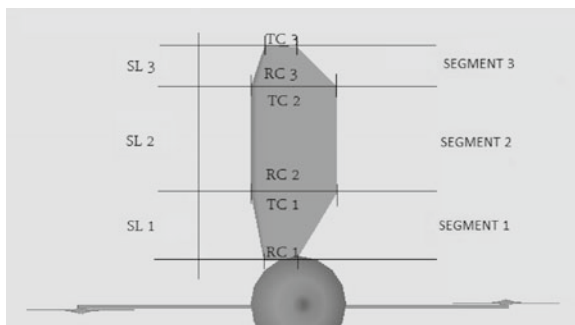


Fig. 16 Wing parameters by sections

Table 3 The relative contribution of changing SL in lift and drag

$\alpha_{AoA} = 15^\circ$			
	SL [ft]	RC [ft]	TC [ft]
Segment 1	1.25	0.6	1.6
Segment 2	2.00	1.6	1.6
Segment 3	par	1.6	1.6
SL ₃ [ft]	ΔSL_{tot} [%]	$\Delta lift_{tot}$ [%]	$\Delta drag_{tot}$ [%]
0.75	–	–	–
1.00	6.25	17.2241	16.9855
1.25	12.5	35.9692	35.6133
1.50	18.75	56.2277	56.0459
1.75	25	78.2494	78.322

that can accurately predict the flight characteristics of nearly any type of aircraft. During the simulation, X-Plane reads in the geometric shape of the aircraft, breaks it down to small elements and uses blade element theory to calculate overall torques and forces that act on the aircraft. This approach provides a good insight into an aircraft's aerodynamics [17].

Developing a new aircraft is achieved in Plane Maker, which comes as the part of X-Plane software package. Plane Maker's primary purpose is creating standard types of aircrafts. On the other hand, it indicates some serious issues in modelling a non standard, miniature type of aerial vehicle. Hence, it was not possible to build an exact copy of the spincopter. Instead, a virtual model in a 1:10 scale has been designed [17].

The spincopter is basically a fixed wing aircraft flying as a rotary wing. Therefore its wings are placed facing the opposite directions, with an angle of attack rotated for 180° . Plane Maker is pri-

Table 4 The relative contribution of changing RC₃ and TC₃ in lift and drag

$\alpha_{AoA} = 15^\circ$			
	SL [ft]	RC [ft]	TC [ft]
Segment 1	1.25	0.6	1.6
Segment 2	2.00	1.6	1.6
Segment 3	0.75	par	par
R/TC ₃ [ft]	$\Delta R/TC_3$ [%]	$\Delta lift_{seg3}$ [%]	$\Delta drag_{seg3}$ [%]
1.6	–	–	–
1.8	12.5	14.0171	15.1899
2.0	25	28.1943	30.7241
2.2	37.5	42.5071	46.6796
2.4	50	56.8701	62.4787

Table 5 The relative contribution of changing α_{AoA} in the lift and drag

$\alpha_{AoA} = \text{par}$			
	$SL [ft]$	$RC [ft]$	$TC [ft]$
Segment 1	1.25	0.6	1.6
Segment 2	2.00	1.6	1.6
Segment 3	0.75	1.6	1.6
$\alpha_{\text{seg3}}^\circ$	$\Delta\alpha_{\text{seg3}}[\%]$	$\Delta\text{lift}_{\text{seg3}}[\%]$	$\Delta\text{drag}_{\text{seg3}}[\%]$
15	–	–	–
12	–20	–14.3672	–26.3446
9	–40	–32.1183	–52.3313
6	–60	–49.9258	–72.0567
3	–80	–67.7013	–85.6821

mary adjusted for designing fixed wing aircrafts, hence the angle of attack can vary by only $\pm 90^\circ$, which is not sufficient [17]. For this reason, only the contributions of the accurately modelled wing (i.e. the one with the correct angle of attack) have been measured. An influence of the mentioned limitation on the flyer's behaviour was the increasing precession in time. Therefore, the behaviour of the spincopter is better at the beginning of simulation.

Airfoil Maker is part of X-Plane which is used for designing airfoils. In order to develop as accurate model as possible, the most similar airfoil to the real one was chosen. It is called *2412 NACA* [21].

4.2 Simulation Results

Due to the mentioned limitations of X-Plane explained in the previous section, an ordinary treatment of the simulation results was not possible. The consequence these limitations have on the lift and drag is a response with plenty of peaks. Hence, to avoid the imperfection of X-Plane, the wing is divided into three segments. Therein, each segment represents one newly designed wing as depicted in Fig. 16, where SL represents the semi-length, RC stands for the root chord and TC is the

Table 6 The relative contribution of changing TC_1 and RC_2 in total lift and drag

$\alpha_{AoA} = 15^\circ$			
	$SL [ft]$	$RC [ft]$	$TC [ft]$
Segment 1	1.25	1.6	par
Segment 2	2.00	par	1.6
Segment 3	0.75	1.6	1.6
par [ft]	$\Delta TC_1, RC_2[\%]$	$\Delta\text{lift}_{\text{tot}}[\%]$	$\Delta\text{drag}_{\text{tot}}[\%]$
1.6	–	–	–
1.3	–18.75	–5.4804	–6.0833
1.0	–37.50	–11.0275	–11.8175
0.7	–56.25	–15.8563	–16.6480
0.4	–75.00	–20.9405	–21.7711

tip chord for each wing. The relevant effect, noticed during the whole newly obtained response, was the maintained ratio of the segments' contribution to the total lift and drag, while keeping the angular velocity constant. Therefore, instead of the absolute values, the relative changes caused by modifications in the wing design were computed.

For this reason, the parameters of the third segment were adapted in several different ways, while 'segment 1' and 'segment 2' were unchanged. The impacts of the changes of semi-length are listed in Table 3.

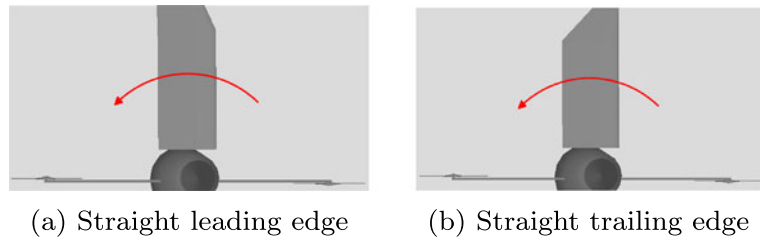
Changes in lift and drag due to alteration of the root and tip chords of the third segment are shown in Table 4.

Finally, an outcome of the changes in the angle of attack of the third segment is given in Table 5.

In order to determine the partial contribution of each wing segment to the overall lift, drag, moment of inertia and mass, some more complex wing shapes were tested. Due to the basic laws of aerodynamics, a lower contribution of the first and second segment in the total lift and drag, as well as in other physical values is expected. For this reason, the tested wing was modelled as depicted in Fig. 17.

Changes in the lift and drag, due to the altering of TC_1 and RC_2 are given in Table 6.

Fig. 17 Tested wing model; changing TC_1 and RC_2


Fig. 18 Tested wing model; changing TC_3 

The shapes given in Table 6, with an invariable parameter TC_1 , ensure a robustness of the wing. Due to its smaller influence on the lift and drag, and the larger influence on the total mass and moment of inertia, for the large range of different materials, according to their density, these shapes might be extremely useful. Altering the conjunction position of the first and second segment, while keeping their sum unchanged, has an insignificant impact in the total lift and drag.

At last, the changes of the tip chord length of the third segment are tested. For this reason, the third segment was modelled with a straight leading edge as shown in Fig. 18a.

The changes in the lift and drag for different TC_3 are given in Table 7.

Another model with straight trailing edge (depicted in Fig. 18b) has caused a large decrease of the lift and an increase of the drag. As such, it won't have any useful impacts in the wing modelling for the spincopter.

The length of the wing has evinced the largest influence on the total lift and drag. On the other hand, it causes a few negative contributions, such as an increase in mass and moment of inertia. To make the spincopter more controllable and due

to the limitations of the actuators, it is useful to decrease the hovering angular velocity (derived in Section 2.2). Therefore, the increase in moment of inertia does not present a problem, as long as the lift grows accordingly.

Increasing the wing width causes a greater rise in drag than lift and is therefore not recommended.

Due to the nonlinearities of the airfoil characteristics, increasing the angle of attack over 13° – 15° , depending on the used airfoil, may cause certain issues (i.e. decreasing L/D ratio) [20].

Applying the results on a real spincopter model, an increased length and a narrowed width of the wing are suggested. Also, an angle of attack of 12° – 13° is recommended since it avoids the fore mentioned nonlinearities. Lowering the parameters TC_1 and RC_2 also has a positive influence on most of the physical indicators, but it reduces the robustness of the aircraft. Hence, decreasing those parameters for 30–40[%] does not cause any real weaknesses (Fig. 19).

5 Spincopter Hardware

Spincopter controller is implemented using an arduino based autopilot board for multirotor crafts. The arduino compatibility makes it easy to

Table 7 The relative contribution of changing TC_3 to the lift and drag

$\alpha_{AoA} = 15^\circ$			
	$SL [ft]$	$RC [ft]$	$TC [ft]$
Segment 1	1.25	1.6	1.6
Segment 2	2.00	1.6	1.6
Segment 3	0.75	1.6	par
par [ft]	$\Delta TC_3 [\%]$	$\Delta lift_{seg3} [\%]$	$\Delta drag_{seg3} [\%]$
1.6	–	–	–
1.3	–18.75	–10.4694	–11.2559
1.0	–37.50	–21.9348	–22.7368
0.7	–56.25	–34.8797	–35.4804
0.4	–75.00	–48.4305	–48.9167

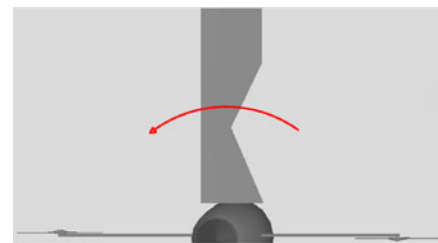
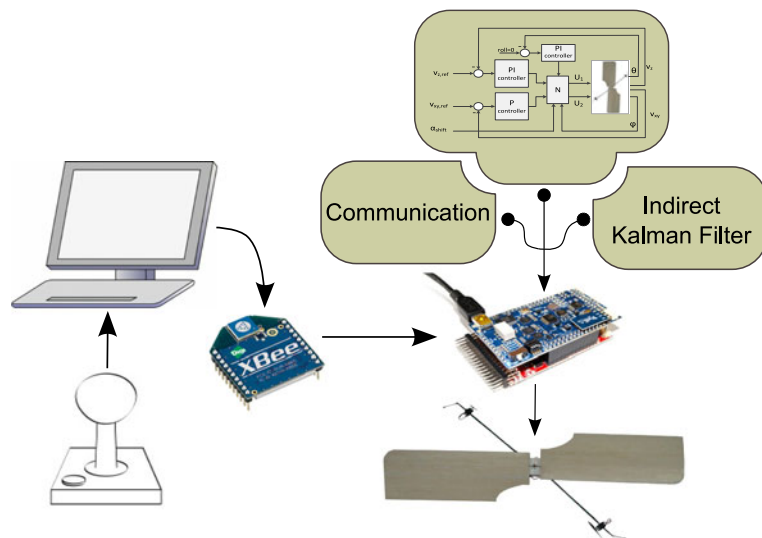
**Fig. 19** The recommended shape of the spincopter's wing

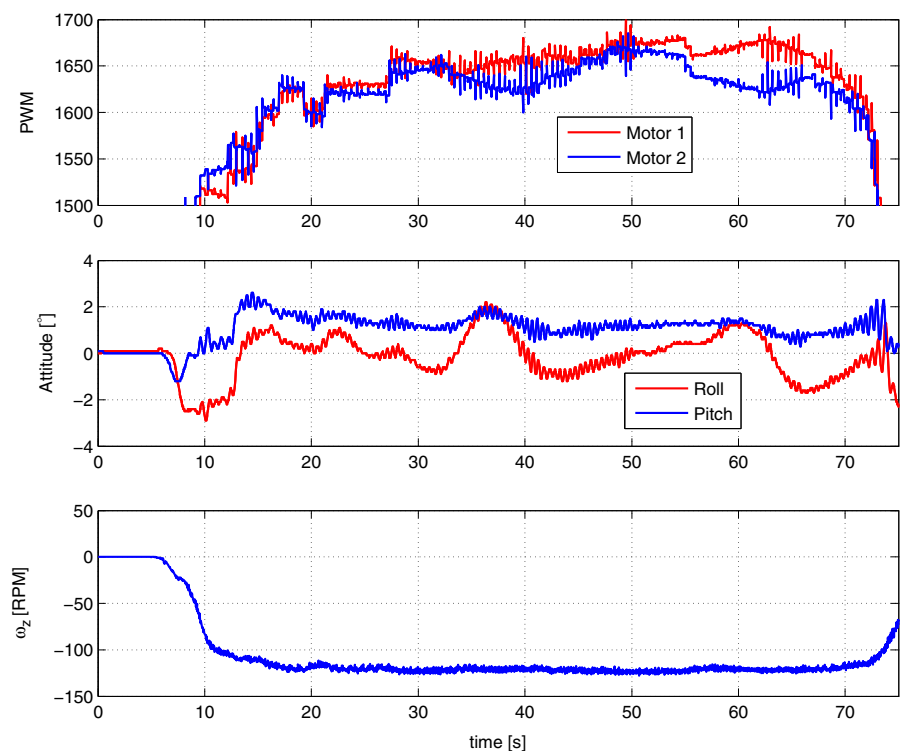
Fig. 20 Spincopter autopilot and communication board



program and adapt to spincopter construction and the onboard sensors (i.e. IMU, compass and sonar) provide feedback for the controller. An indirect form of Kalman filter is used to fuse the information from different sensors. Spincopter is controlled through a joystick, connected to a stan-

dard PC platform. The communication between the PC and the autopilot board is implemented using standard XBee modules. The communication provides the basic control and telemetry data. A pictogram description of autopilot implementation is shown in Fig. 20.

Fig. 21 Roll stabilization results



6 Experimental Results

This section shows the experimental results of a manual test flight where the operator controls the height and the position of the aircraft, with an enabled roll stabilization loop controller. The video recording of this test flight can be found here <http://youtu.be/54Q2bL8XaAE>. The results show the effectiveness of the pulsation control technique proposed in Section 2.2. Implementation of a fully autonomous flight requires implementing additional position and height feedback signals.

As far as the roll stabilization loop is concerned: the results are shown in Fig. 21. The results show that by using a simple PI we were able to stabilize the aircraft within a satisfying 2° .

PWM outputs show how the difference in the speed of each motor produces the necessary stabilization torque. Furthermore, actual PWM difference is within 6–8% of total PWM span and thus causes a very small disturbance in height control. In addition to that, it leaves enough space for the pulsation algorithm (i.e. position control) to successfully control the spincopter in x - y plane.

The last plot in Fig. 21 shows the rotation speed of the aircraft. The aircraft takes off at approximately 120RPM rotation speed and at the 65–70% of total applied voltage. This leaves enough room to achieve successful motions in 3D space.

7 Conclusion

An UAV concept based on two rotating wings is presented herein. DeVised mathematical model of flight dynamics demonstrate inherent stability of the UAV. Movements in vertical and horizontal directions are produced by two actuators, placed symmetrically with respect to the center of gravity of the vehicle. While control of vertical position is very simple and requires only change in propulsion of both actuators, control algorithm for horizontal position is more complex as it is based on actuator pulsations. Since propulsion is produced by brushless dc motors, influence of the motor dynamics on the vehicle performance has been investigated. Simulation results demonstrate that the most efficient pulsation period is 360° and it is not dependent on the motor dynamics. In the

last part of the paper recommendations regarding the wing shape are given. The wing is divided into three segments and influence of each segment on lift and drag are tested by simulations. The future work is directed towards sensor data fusion and interpretation that should finally lead to realization of autonomous flight of the proposed concept vehicle.

Acknowledgements Research work presented in this paper is part of projects 036-0363078-3016 ‘Planning and scheduling tasks in robotics and autonomous systems’, financed by the government of Republic of Croatia, and REGPOT-CT-2011-285939-ACROSS ‘Center of research excellence for advanced cooperative systems’ financed by European Union.

References

1. Chabak, K.D.: Conceptual study of rotary-wing micro-robots. Ph.D. Thesis, AFIT/GE/ENG/08-03, Air Force Institute of technology (2008)
2. Hu, H., Clemons, L., Igarashi, H.: An experimental study of the unsteady vortex structures in the wake of a root-fixed flapping wing. *Exp. Fluids* **51**(2) 347–359 (2011)
3. Wood, R., et al.: Progress on “pico” air vehicles. In: Proceedings of International Symposium on Robotics Research, pp. 1–16 (2011)
4. Ellington, C.: The novel aerodynamics of insect flight: applications to micro-air vehicles. *J. Exp. Biol.* **202**, 3439–3448 (1999)
5. Fregene, K., Bolden, C.: Dynamics and control of a biomimetic single-wing nano air vehicle. In: Proceedings of American Control Conference (ACC), pp. 51–56 (2010)
6. Thipyopas, C., et al.: Application of electro-active materials to a coaxial-rotor nav. In: Proceedings of International Micro Air Vehicle conference, pp. 21–26 (2011)
7. Sane, S.P.: The aerodynamics of insect flight. *J. Exp. Biol.* **206**, 4191–4208 (2003)
8. Newman, B., Savage, S., Schouella, D.: Model tests of a wing section of an aescna dragonfly. In: Scale Effects in Animal Locomotion, pp. 445–477 (1977)
9. Azuma, A., Okuno, Y.: Flight of a samara, *alsomitra macrocarpa*. *J. Theor. Biol.* **129**(3), 263–274 (1987)
10. Azuma, A., Yasuda, K.: Flight performance of rotary seeds. *J. Theor. Biol.* **138**(1), 23–53 (1989)
11. Lentink, D., Dickson, W., van Leeuwen, J., Dickinson, M.: Leading-edge vortices elevate lift of autorotating plant seeds. *Science* **324**(5933), 1438–1440 (2009)
12. Varshney, K., Chang, S., Wang, J.: The kinematics of falling maple seeds and the initial transition to a helical motion. *Nonlinearity* **25**, C1–C8 (2012)
13. Ramamurthi, R., et al.: Computational fluid dynamics study of unconventional air vehicle configurations.

- In: Proceedings of 19th Bristol International Conference on Unmanned Air Vehicle Systems, pp. 1–18 (2004)
14. Liu, Z., Moschetta, J.-M.: Rotary vs. flapping-wing nano air vehicles: Comparing hovering power. In: Proceedings of The European Micro Aerial Vehicle Conference, pp. 21–27 (2009)
 15. Ulrich, E.R., Humbert, J.S., Pines, D.J.: Pitch and heave control of robotic samara micro air vehicles. *J. Aircr.* **47**(4), 1290–1299 (2010)
 16. Kellogg, J.C., et al.: Design and development of the samara stop-rotor hybrid micro air vehicle. In: Proceedings of 20th Bristol International Conference on Unmanned Air Vehicle Systems, pp. 129–135 (2005)
 17. Orsag, M., Bogdan, S., Haus, T., Bunic, M., Krnjak, A.: Modeling, simulation and control of a spincopter. In: IEEE International Conference on Robotics and Automation, ICRA 2011, Shanghai, China, pp. 2998–3003, 9–13 May 2011. IEEE (2011)
 18. Bramwell, A.R.S., Done, G., Balmford, D.: *Bramwells Helicopter Dynamics*. American Institute of Aeronautics and Astronautics (2001)
 19. Hummel, S.A.: *Frisbee Flight Simulation and Throw Biomechanics*. Master's thesis, University of California Davis (2003)
 20. Leishman, J.G.: *Principles of Helicopter Aerodynamics*, 2nd edn. Cambridge University Press, New York, NY (2006)
 21. Eastman, K.E.W., Jacobs, N., Pinkerton, R.M.: The characteristics of 78 related airfoil sections from tests in the variable-density wind tunnel. Report no. 460. Tech. Rep. (1933)